3D osteocyte lacunar morphometry of human bone biopsies with high resolution microCT: from monoclonal gammopathy to newly diagnosed multiple myeloma

Inés Moreno-Jiménez[1*], Sharen Heinig[1], Unai Heras[2], Daniela Simone Maichl[3], Susanne Strifler[3], Ellen Leich-Zbat[3,4], Stéphane Blouin[5], Peter Fratzl[1], Nadja Fratzl-Zelman[5], Franziska Jundt[3,6*#], Amaia Cipitria[1,2,7*#]

[1] Max Planck Institute of Colloids and Interfaces, Department of Biomaterials, 14476 Potsdam, Germany

[2] Group of Bioengineering in Regeneration and Cancer, Biodonostia Health Research Institute, 20014 San Sebastian, Spain.

[3] Department of Internal Medicine II, University Hospital Würzburg, 97080 Würzburg, Germany

[4] Institute of Pathology, University of Würzburg, 97080 Würzburg, Germany

[5] Ludwig Boltzmann Institute of Osteology at the Hanusch Hospital of OEGK and AUVA Trauma Centre Meidling, Vienna, Austria.

[6] Comprehensive Cancer Center Mainfranken, 97080 Würzburg, Germany

[7] IKERBASQUE, Basque Foundation for Science, 48009 Bilbao, Spain.

(*) Correspondence to: ines.moreno@mpikg.mpg.de; Jundt_f@ukw.de; amaia.cipitria@mpikg.mpg.de; amaia.cipitria@biodonostia.org

(#) These authors contributed equally to this work

Abstract

Osteocytes are bone-embedded cells connected via canaliculi and they regulate the bone resorption/formation balance. Osteocyte function is altered in skeletal disorders including cancer. Multiple myeloma (MM) is a hematological malignancy, whereby plasma cells disrupt the bone homeostasis and induce excessive resorption of the mineralized extracellular matrix (ECM), as evidenced by clinical computed tomography (CT). However, morphometric analyses of the mineralized ECM and bone microporosity are not yet performed in patients with MM, nor in the precursor conditions of monoclonal gammopathy of undetermined significance (MGUS) and smoldering MM (SMM). Here, we characterize changes in 3D osteocyte lacunar morphology in bone biopsy samples obtained from patients with MGUS, SMM and newly diagnosed MM, using high resolution microCT. In the small lacunae 20-900 μm^3 range, we found a trend for lower lacunar density and increasing 50% cutoff of the lacunar volume cumulative distribution for diseased samples. In the larger lacunae 900-3000 μm^3 range, we found significantly higher lacunar density and microporosity in the MM group compared to the MGUS/SMM group. Regarding the shape distribution, the MGUS/SMM group showed a trend for flatter, more elongated and anisotropic osteocyte lacunae compared to the control group, though the differences were not statistically significant. Altogether, our findings suggest that osteocytes in human MM bone disease undergo changes in their lacunae morphology, which could be an indicator for impaired bone quality. Future studies are needed to show whether these are consistent within comparable anatomical sites and could serve as a diagnostic or prognostic marker.

Keywords

Osteocyte lacuna, Morphometry; High resolution microCT; Human bone biopsy; Multiple myeloma (MM); Monoclonal gammopathy of undetermined significance (MGUS); Smoldering myeloma (SMM)

1. Introduction

Bone is a dynamic organ which, besides providing structural support to the body, acts as a metabolic and hematopoietic reservoir. In addition to the vast number of cell types and biomolecules involved in the bone organ, bone extracellular matrix (ECM) also plays a crucial role in maintaining bone homeostasis [1]. Bone ECM is composed of an inorganic (hydroxyapatite mineral crystals) and an organic phase (primarily of collagen type I and proteoglycans), which provide mechanical strength. Osteocytes are bone-embedded cells, connected via dendrites in a lacuno-canalicular network (LCN). They act as local sentinels in response to external stimuli and regulate the balance between bone resorption/formation [2]. Hence, factors such as collagen, mineral crystals and osteocyte LCN affecting bone matrix organization will have an impact on bone physiology

Lacunar volume, shape and density has been shown to be influenced by changes of the surrounding environment, either mechanically or chemically, and by aging or disease. Larger lacunae have been observed after exposing mice to non-gravity [3] or after treatment with glucocorticoid to slow down bone metabolism [4]. Smaller lacunar size and density have been observed in rodent models of aging [5]. Significantly lower osteocyte lacunar volume was found in an osteoporotic rat model compared to healthy controls and the effect of different anti-resorptive drugs in intracortical microporosities was evaluated [6]. In humans, decreasing lacunar density was observed with aging, while a significantly higher density was found in osteoporotic bone compared to controls [7]. A recent study with human bone biopsy samples of healthy individuals across the life span revealed decreasing osteocyte lacunae density and porosity with aging before the peak bone mass at 30 years, which then stabilized or even increased after this age [8]. Mineralized osteocyte lacunae (micropetrosis) have been found with aging and osteoporosis, attributed to osteocyte apoptosis, which was improved with bisphosphonates [9]. Lacunar shape changes have also been associated with aging, becoming smaller and more spherical with increasing age [10]. Such osteocyte morphological changes are responsible for lower local bone tissue strains and affect bone mechanosensitivity [11]. In osteogenesis imperfecta, a higher density of osteocyte lacunae per unit volume [12–14], with more spherical shape compared to the ellipsoidal lacunae in control mice was observed [14].

In cancer, osteocytes, as well as osteoblasts and osteoclasts, communicate with tumor cells and this generates a microenvironment that supports cancer cell growth and stimulates bone destruction [15]. Interactions between breast and prostate cancer cells and osteocytes affect the

88 cancer cell migration and invasion potential and contribute to the establishment and
89 progression of bone metastasis [16,17]. Also, breast cancer cells induce osteocyte apoptosis and
90 alter osteocyte function [18]. Recently, a study of osteotropic cancers in rodents revealed that
91 the spatial distribution of cortical bone microporosity, osteocyte lacunae volume and the LCN
92 characteristics are influenced by the presence of tumor cells in osteosclerotic and osteolytic
93 lesions [19]. Taken together, changes in bone microstructure and the LCN play a role in
94 different types of bone metastasis. Ultrastructural characterization will help understand how
95 different tumor cells interact with osteocytes, causing characteristic footprints in the bone
96 microstructure and impairing bone integrity and physiology.
97
98 An example of an incurable malignancy of the bone marrow is multiple myeloma (MM), in
99 which plasma cells disrupt the bone homeostasis towards excessive bone resorption [20].
100 Patients diagnosed with MM develop symptoms termed CRAB: hypercalcemia, renal
101 insufficiency, anemia and osteolytic bone lesions[21]. Initially, an abnormal proliferation of
102 plasma cells (< 10%) producing aberrant antibodies in serum (< 3 g/dL) is clinically
103 identified as benign, termed 'monoclonal gammopathy of underdetermined significance'
104 (MGUS). When MGUS continuously progresses into the next stage, named smoldering
105 multiple myeloma (SMM), CRAB symptoms are not yet present. However, SMM represents
106 a broad biological spectrum: (i) clinical cases which do not progress into symptomatic
107 disease over years, and (ii) high-risk cases in which patients have an 80 % chance of disease
108 progression within two years [22]. To better define those high-risk SMM, who require
109 immediate intervention to prevent end-organ damage, particularly to bone and kidney, the
110 International Myeloma Working Group published updated the criteria for the diagnosis of
111 MM [23]. Validated biomarkers were included, such as the detection of one or more focal
112 lesions by magnetic resonance imaging (MRI) and diffuse infiltration (≥ 60%) of clonal
113 plasma cell in the bone marrow even without bone lytic lesions.
114
115 MM cells alter the bone marrow environment by releasing signals that promote osteoclast
116 activity, while inhibiting osteoblast function [24,25]. Interestingly, MM bone lesions rarely heal,
117 even after years of patients being in complete disease remission [26]. There is evidence that
118 MM cells also target osteocytes by enhancing cell apoptosis and expression of sclerostin, an
119 inhibitor of bone formation [27]. Even though MM cells directly interact with osteocytes and
120 vice versa, the consequences of these interactions on the local bone microstructure and the
121 role of the ECM in disease development are largely unknown [27]. Our group has shown local

122 ECM alterations with active erosion sites, irregular shaped osteocyte lacunae and altered
123 osteocyte LCN architecture, using an early MM mouse model [28]. Thus, examining the bone
124 microstructure in MM and the precursor conditions MGUS and SMM would provide insights
125 in the pathophysiology of this disease. It is currently unknown how human bone ECM is
126 affected at the ultrastructural level in MGUS, SMM and newly diagnosed MM bone disease.
127 The aim of this study is to quantitatively characterize changes in osteocyte lacunae and
128 micropores from MGUS to newly diagnosed MM, using ex vivo human bone biopsies.
129 Determination of these changes could help identifying diagnostic or prognostic indicators for
130 the progression of MM bone disease.
131
132 **2. Results**
133 **2.1 Clinical data and patient history**
134 Clinical data from patients from the University Hospital Würzburg and parameters describing
135 bone metabolism are compiled in Tables 1-3. The cohort included patient-derived bone
136 biopsy samples with the precursor condition MGUS (Table 1), SMM (Table 2), and newly
137 diagnosed MM (Table 3). The revised International Staging System for Multiple myeloma (r-
138 ISS) was used to stratify patients with respect to their survival [29]. Control samples obtained
139 from the University Hospital Würzburg and from the Ludwig Boltzmann-Institute of
140 Osteology Vienna are compiled in Table 4. Only biopsy samples containing sufficient
141 trabecular bone were included.
142
143 Patients with MGUS showed no detectable osteolytic bone lesions by low-dose CT scans.
144 One patient with MGUS received denosumab for four months. In this case, we cannot
145 exclude that the anti-resorptive treatment interfered with the bone ultrastructure. Similarly,
146 the two patients classified as SMM exhibited no signs of osteolytic lesions by low-dose CT
147 scans at the time of biopsy. The disease stage of SMM was based on the percent of bone
148 marrow infiltration of $CD138^+$ cells, above 10%. Patients classified as MM had a bone
149 marrow infiltration of $CD138^+$ cells between 60-90% (4 out of 6), a ratio of the involved to
150 the uninvolved free light chain in the serum (sFLC) of >100 (2 out of 6), and/or local or
151 disseminated lytic lesions, as well as reduced bone mineral density (4 out of 6). All bone
152 turnover markers (phosphate, calcium, alkaline phosphatase) were within normal ranges.
153 Anti-resorptive therapy with the bisphosphonate zoledronic acid had been administered to
154 one MM patient for one month before the biopsy was taken. We assume that the single dose
155 of the bisphosphonate did not affect bone ultrastructure in such short time.

156 **2.2 Immunohistochemical (IHC) and microcomputed tomography (microCT) overview**
157 **analysis**
158 As part of the standard clinical practice, bone biopsies were processed for
159 immunohistochemical (IHC) analysis for CD138 staining, to detect the clonal bone marrow
160 plasma cells and quantify the percent of bone marrow infiltration of $CD138^+$ cells. Fig. 1a-c
161 shows representative samples of MGUS, SMM and newly diagnosed MM patients with
162 <10% for MGUS and >10% for SMM and MM patients. Bone biopsy samples containing
163 sufficient trabecular bone were scanned with microcomputed tomography (microCT). 3D
164 renders of representative images are shown in Fig. 1d-f. Quantification of trabecular
165 thickness distribution is shown in Fig. 1g-j. No differences between the three groups were
166 observed in the macroscopic trabecular bone architecture, indicating the resolution might
167 limit the ability to detect pathological changes.
168
169 **2.3 Bone ultrastructure and segmentation of osteocyte lacunar microporosity**
170 We next investigated the bone ultrastructure with a focus on the osteocyte lacunar
171 microporosity. High resolution microCT scans (voxel size 1-2 μm) were performed on
172 smaller volumes of interest (VOI) and the empty cavities within mineralized tissue
173 corresponding to osteocyte lacunae were segmented. Cavities smaller than 20 μm^3 and larger
174 than 3000 μm^3 were considered cracks or artifacts and excluded from the analysis. VOI of
175 representative samples and the segmented osteocyte lacunar microporosity are visualized in
176 Fig. 2.
177
178 **2.4. Osteocyte lacunar volume distribution and microporosity analysis**
179 We characterized the osteocyte lacunar volume distribution, first as a frequency distribution
180 (Fig. 3) and then as a cumulative distribution (Fig. 4). To plot the lacunar volume frequency
181 distribution, all lacunae within one sample were stratified according to volume intervals. For
182 a discrete lacunar volume interval, we quantified the number of osteocyte lacunae (Lc.N.) for
183 that given size, normalized to the trabecular bone volume and excluding lacunar total volume
184 (Tb.TV-Lc.TV), to account for samples of different size. Two separate lacunar volume ranges
185 were investigated: small lacunae 20-900 μm^3 (Fig. 3a-c) and larger lacunae 900-3000 μm^3
186 (Fig. 3d-f). Control samples (Fig. 3a, d) were compared with MGUS, SMM (Fig. 3b, e), and
187 MM (Fig. 3c, f).
188

In the small lacunae range 20-900 μm^3, we observed a comparable distribution in the different groups, with the exception of sample #MM 3, with significantly higher number of osteocyte lacunae compared to other samples within the MM group (Fig. 3c). In contrast, in the larger lacunae range 900-3000 μm^3, we observe a significantly higher number of lacunae for the MM group (Fig. 3f) compared with MGUS (Fig. 3d) and SMM (Fig. 3e) groups

When comparing both ranges, we observed a larger number of small osteocyte lacunae (Fig. 3a-c) compared to larger lacunae (Fig. 3d-f). This motivated a more detailed lacunar volume cumulative distribution analysis (Fig. 4), where the lacunar number (Lc.N) was plotted as a cumulative curve. The 50% cutoff indicates that half of all osteocyte lacunae within one sample are below that specific volume interval (x-axis). In the control group (Fig. 4a), the 50% cutoff is heterogeneous: samples #control 1, #control 3 and #control 4 have 50% of the lacunae with volumes around 140-170 μm^3, while sample #control 2 has the highest volume with 270 μm^3. In the MGUS/SMM group (Fig. 4b), the 50% cutoff ranges from 170-210 μm^3, except sample #SMM 2 with the smallest cutoff at 140 μm^3. In the MM group (Fig. 4c), the 50% cutoff varies from 150-220 μm^3, with clearly lower values for the biopsies of patients without bone osteolytic lesions (#MM 3 and #MM 6). In conclusion, we observe a trend for increasing 50% cutoff for more advanced disease, indicating that the sum volume of the smallest 50% lacunae account for a larger volume as the disease progresses (Fig. 4c).

Finally, we calculated the lacunar density as the total number of osteocyte lacunae (Lc.TN) normalized to the trabecular bone volume and excluding lacunar total volume (Tb.TV-Lc.TV), in other words, the summation of the osteocyte lacunar volume frequency distribution (Fig. 3). This was done for both ranges separately, small lacunae 20-900 μm^3 (Fig. 5a) and larger lacunae 900-3000 μm^3 (Fig. 5b). In the small lacunae range, the mean for the control samples was 29809 +/- 11314 lacunae/mm^3, for MGUS/SMM 18165 +/- 3278 lacunae/mm^3 and for MM 20502 +/- 13827 lacunae/mm^3. No significant differences were observed in the small lacunae range, although there was a clear trend for lower lacunar density for diseased samples (MGUS/SMM and MM) compared to the controls. However, in the larger lacunae range 900-3000 μm^3 (Fig. 5b), significantly higher lacunar density was found in the MM group compared to the MGUS/SMM group.

We also calculated the microporosity as the lacunar total volume (Lc.TV) divided by trabecular total bone volume (Tb.TV) for each group. This was done for both ranges separately, small lacunae 20-900 μm^3 (Fig. 5c) and larger lacunae 900-3000 μm^3 (Fig. 5d). No significant differences were observed in the small lacunae range. However, in the larger lacunae range, significantly higher microporosity was found in the MM group compared to the MGUS/SMM group. This is consistent with the observations of lacunar volume frequency distribution (Fig. 3f) and lacunar density (Fig. 5b).

2.5 Osteocyte lacunar morphological analysis

We performed a lacunar morphological analysis in the small lacunae 20-900 μm^3 range, for each group control, MGUS/SMM and newly diagnosed MM. Based on previous analogous analysis [30,31], we investigated the distribution of lacunar flatness, elongation and anisotropy. To do so, the principal eigenvalues for each osteocyte lacunae were obtained: EV1, EV2 and EV3. The morphological parameters were calculated as follows: lacuna elongation as EV2/EV1 (ratio of medium to largest eigenvalue) ranging from lower values for elongated and 1 for spherical (Fig. 6a-d); lacuna flatness as EV3/EV2 (ratio of smallest to medium eigenvalue) ranging from 0 for flat to 1 for spherical (Fig. 6e-h); and lacuna anisotropy as 1-EV3/EV1 (one minus the ratio of smallest to largest eigenvalue) ranging from 0 for isotropic/spherical to 1 for highest anisotropy (Fig. 6i-l). The fraction of lacunar number (Lc.N) normalized against lacunae total number (Lc.TN) in each sample is shown for each group control (Fig. 6a, e, i), MGUS/SMM (Fig. 6b, f, j) and MM (Fig. 6c, g, k). The median of all lacuna elongation values for each sample are shown in Fig. 6d; similarly, for flatness in Fig. 6h and anisotropy in Fig. 6l.

Lacuna flatness in MGUS/SMM and newly diagnosed MM groups exhibit a broader spread of the distribution compared to the control group, with a shift towards lower values (flatter shapes). Regarding lacuna elongation and anisotropy, the spread of the distribution for the three groups is comparable. A trend for lower values for lacuna elongation (more elongated) and higher values for lacuna anisotropy (more anisotropic) is observed in the MGUS/SMM group compared to the control group, as shown by the curves and the by the median values. However, the differences of the median values are not significant.

3. Discussion

254 Osteocyte function is altered in skeletal disorders including cancer. In MM bone disease,
255 osteolytic lesions are frequently diagnosed in clinical CT scans, however, changes in the
256 mineralized ECM and morphometric analyses of bone microporosity in bone biopsies are not
257 routinely analyzed. To our knowledge, here we present the first quantitative investigation of
258 osteocyte lacunae volume and shape distribution in human bone biopsy samples obtained
259 from MGUS, SMM and newly diagnosed MM patients using high resolution microCT (voxel
260 size 1-2 μm).
261
262 Our data demonstrate altered lacunae volume and shape distribution with MGUS, SMM and
263 newly diagnosed MM. Specifically, we found a significantly higher number of larger lacunae
264 in the 900-3000 μm^3 range in the MM group compared to the MGUS/SMM groups, as
265 reflected in an increase in lacunar volume frequency distribution (Fig. 3f) and lacunar density
266 (Fig. 5b). The study also found significantly higher microporosity for the larger lacunae range
267 in the MM group compared to the MGUS/SMM group (Fig. d), consistent with the
268 observation of an increase in lacunar volume frequency distribution. One limitation of this
269 analysis is that the larger lacunae in the 900-3000 μm^3 range probably includes both enlarged
270 osteocyte lacunae and other pathological features in the form of micropores.
271
272 In the small lacunae 20-900 μm^3 range, the lacunar density for control samples with 29809
273 +/- 11314 lacunae/mm^3 (Fig. 5a) is in the range previously reported in the literature for 3D
274 analysis of osteocyte morphometry in healthy transiliac bone biopsies [32], which confirms the
275 validity of our analysis. Interestingly, there was a trend for lower lacunar density for diseased
276 samples (MGUS/SMM and MM) compared to the controls, though the differences were not
277 significant (Fig. 5a). This could be indicative of micropetrosis, i.e. osteocyte lacunae
278 mineralization following osteocyte apoptosis [33,34]. Since a lower lacunar density can
279 distinguish healthy, osteoporotic and bisphosphonate-treated osteoporotic patients, it is
280 currently being considered as a novel bone microstructural maker of impaired bone quality [33].
281 Finally, we observed a trend for increasing values of the 50% cutoff in the lacunar volume
282 cumulative distribution for more advanced disease, showing that the sum volume of the
283 smallest 50% lacunae account for a larger volume as the disease progresses (Fig. 4).
284
285 In terms of shape distribution, the MGUS/SMM group showed a trend for lower lacuna
286 flatness (flatter), lower lacuna elongation (more elongated), and higher lacuna anisotropy

287 (more anisotropy) compared to the control group (Fig. 6). Altogether, the findings of a trend
288 for lower lacunar density and increasing 50% cutoff of the lacunar volume cumulative
289 distribution for diseased samples in the small lacunae 20-900 μm^3 range, together with
290 significantly higher lacunar density and microporosity for the MM group in the larger lacunae
291 900-3000 μm^3 range, suggest that the osteocytes in MM bone disease and the precursor
292 conditions MGUS/SMM are undergoing changes in their lacunae morphology.
293
294 In a recent study in immunocompetent mice, breast and prostate cancer cells were
295 intratibially injected and the changes in the osteocyte LCN induced by tumor cells were
296 analyzed by histology, microCT imaging and confocal laser scanning microscopy [27].
297 Interestingly, large lacunae and vascular canals were not observed in the proximity of
298 osteolytic lesions, whereas these changes occurred in osteosclerotic lesions adjacent to
299 prostate cancer cells [27], indicating that changes of osteocyte LCN characteristics are tumor
300 type-specific. In our study of biopsy samples from patients with MM and the precursor
301 conditions, we observed a significantly higher number of larger lacunae in the MM group
302 compared to the MGUS/SMM groups. These changes may be related to the presence of
303 osteocytic osteolysis [35], a process that involves osteocytes mobilizing calcium and phosphate,
304 using carbonic anhydrase and vacuolar ATPase to demineralize the bone matrix, and digest
305 protein using matrix metalloproteases and tartrate-resistant acid phosphatase (TRAP) [27,36–38].
306 In the above-mentioned mouse model [27], TRAP-positive osteocytes in combination with large
307 lacunae were detected in osteosclerotic regions of breast and prostate infiltrated bones,
308 indicating that this mechanism could contribute to the observed increase in lacunae volume
309 [27,36–38]. Whether osteocytic osteolysis plays a role in the progression from healthy to
310 MGUS/SMM to MM bone is not known and warrants further studies. Moreover, since the
311 osteocyte remodeling function affects the lacunae morphology and the LCN architecture, it is
312 likely that changes in the latter are indicators for impaired bone remodeling activity.
313
314 In order to understand the implications of altered lacunae volume and shape distribution in
315 MM, future studies should consider several factors. First, there is a need for more bone
316 biopsies of sufficient quality to obtain a larger sample size and validate the findings of this
317 study. Second, it is important that the bone biopsies are obtained from comparable anatomical
318 sites to minimize the natural osteocyte volume and shape variation within healthy bone [8,32,39].
319 Additionally, to further investigate the relationship between osteocyte lacunae and MM,

320 researchers should increase the volume of interest scanned at high resolution (1 µm voxel
321 size or lower) for instance using phase-contrast synchrotron microCT. Furthermore, the
322 implementation of deep learning algorithms could facilitate the analysis of large numbers of
323 osteocyte lacunae and improve the accuracy of image analysis. In addition to lacunar
324 abnormalities, quantitative analysis of alterations in the LCN (i.e. canalicular density,
325 connectivity) should be explored in future studies. Finally, investigating clinical bone
326 endocrine parameters such as parathyroid hormone, bone-specific alkaline phosphatase,
327 amino-terminal pro-peptide of type I procollagen, carboxy-terminal telopeptide of type I
328 collagen, TRAP5b or fibroblast growth factor-23 produced by osteocytes, in relation to
329 calcium and phosphorus and in relation to lacunae morphology, could provide valuable
330 insights into the pathogenesis of MM and link this to the clinical setting [40]. Measuring serum
331 parameters may be easier than performing microCT analysis of osteocyte lacuna, and
332 incorporating these measurements into future studies could provide a more comprehensive
333 understanding of the impaired bone remodeling capacity in MM bone disease. Additionally,
334 the use of animal models of MM and other bone diseases may provide a valuable tool for
335 investigating the mechanisms underlying the observed alterations in osteocyte lacunae
336 morphology and other aspects of bone ultrastructure, such as LCN architecture, bone
337 composition, and micro- and nanoscale organization of the organic and inorganic matrix. We
338 recently established a MM bone disease model for ultrastructural characterization of the ECM
339 in early stages of the disease [28,41–43]. In skeletally mature mice, we detected a disorganized
340 osteocyte LCN architecture, and irregular-shaped osteocyte lacunae in MM-injected bones
341 after 21 days [28]. This model will help to characterize early on the development and
342 progression of ultrastructural changes of MM bone disease.
343
344 Taken together, these findings suggest that altered lacunae volume and shape distribution
345 may play a role in the pathogenesis of MM and the precursor conditions MGUS and SMM,
346 and could potentially serve as a diagnostic or prognostic marker for the disease. Further
347 studies are needed to explore the clinical implications of these results and to determine
348 whether targeting lacunar abnormalities could be a viable therapeutic approach for MM.
349
350 **4. Materials and methods**
351 **4.1 Patient sample collection and clinical evaluation**
352 The purpose of this study was to determine whether changes in osteocyte lacunae volume and
353 shape distribution could be detected in mineralized bone biopsy samples from patients with

354 MGUS, SMM and newly diagnosed MM. MGUS (n=3), SMM (n=2) and symptomatic MM
355 (n=6) were diagnosed following the revised international staging system [23]. Clinical data
356 from patients including reports of the low-dose CT scans are given in Tables 1-3. The
357 investigators who performed the bench studies were blind to the patient information. This
358 study was approved by the Ethics Committee of the University of Würzburg, Germany
359 (82/20-am).
360
361 As control bone biopsy samples, two different data sets were used (Table 4). One Jamshidi
362 bone biopsy sample (2 mm diameter) was obtained from a patient of the University Hospital
363 Würzburg with myelodysplastic syndrome. Three samples (5 mm diameter) were obtained
364 from an earlier study [8] from autopsies at the Ludwig Boltzmann-Institute of Osteology
365 Vienna. Osteocyte lacunae characteristics were re-evaluated in the current study. For all
366 control and disease bone biopsy samples, the trabecular bone compartment was analyzed and
367 the cortical bone was excluded. Only biopsy samples containing sufficient trabecular bone
368 were considered.
369
370 The patient clinical data (Tables 1-3) include: biopsy number, disease stage (MGUS, SMM or
371 newly diagnosed MM), age, gender, immunoglobulin subtypes (heavy and light chains)
372 secreted by malignant plasma cells, revised International Staging System (r-ISS), cytogenetic
373 risk, M-protein secreted by plasma cells at time of diagnosis (g/L), heavy chain (mg/dL),
374 involved serum free light chain (sFLC) (mg/L), ratio (involved/uninvolved sFLC), bone
375 marrow infiltration (%) based on immunohistochemistry Syndecan-1 (CD138) with >60%
376 corresponding to newly diagnosed MM, computed tomography findings of osteolytic lesions,
377 hemoglobin (g/dL), creatinine (mg/dL) and cytogenetic alterations by fluorescence in situ
378 hybridization (FISH), which allows for detection of genetic changes which are relevant for
379 the ISS stage. In addition, parameters describing the bone metabolism include: calcium
380 (mmol/L), alkaline phosphatase (U/L), phosphate (mmol/L) and finally, bone anti-resorption
381 treatment ongoing at the time of biopsy.
382
383 **4.2 Immunohistochemical detection of CD138 on decalcified bone paraffin sections**
384 Paraffin embedded human specimens were retrospectively collected from formalin-fixed
385 paraffin-embedded tissue of anonymized samples, archived at the Institute of Pathology,
386 University of Würzburg. Shortly, Jamshidi bone biopsy samples that were derived from the
387 clinical department of the University of Würzburg were fixed for 24 h in formalin,

decalcified for 24 h at 37°C using an EDTA-based approach, dehydrated with alcohol and xylene and then embedded in paraffin.

For the immunohistochemical detection of CD138/Syndecan-1 expression, sections were deparaffinized. The tissue was hybridized with an antibody against CD138/Syndecan-1 (clone MI15, mouse, #M7228, Agilent, Santa Clara, CA, USA), following standard procedures by automated processing using the Tecan Evo Freedom stainer and the Dako Advance system according to the manufacturer's protocol.

4.3 Microcomputed tomography (microCT): image acquisition

Specimens were scanned using an EasyTom micro/nano tomograph (RX solutions, France). Low resolution scanning parameters were: 107 kV, 93 µA, 7 µm voxel size, frame rate of 3, average frame of 5. High resolution scanning parameters were: 60 kV, 124 µA, 1-2 µm voxel size, frame rate of 1, average frame of 5. Reconstruction of the 1120 projections/scan were performed using RX Solutions X-Act software.

4.4 Low resolution microCT: image analysis

The overall bone biopsy morphology with particular focus on trabecular bone thickness was analyzed with Dragonfly v.2022.1 software (Object Research Systems Inc., Montreal, Canada, 2022). Low resolution microCT stack images (voxel size of 7 µm) were segmented using Otsu thresholding ("denoising" of these microCT images and objects was not necessary). A mesh was then created from each individual region of interest (ROI) of the trabecular bone.

The trabecular bone strut thickness was automatically measured from each mesh by Dragonfly software. For this, we calculated the mean and standard deviation values of about 3-5.5 10^6 local vertices created between boundary points of each overall mesh. The software calculated these vertices as diameters of hypothetical spheres that fit within each boundary points of the mesh. The trabecular bone strut thickness distribution is depicted with a color code for each biopsy and as a histogram.

4.5 High resolution microCT: image analysis

<u>4.5.1 Segmentation of osteocyte lacunae</u>

420 The stack of high resolution microCT images (1-2 µm voxel size) was segmented using Otsu
421 thresholding in Dragonfly. For these images, noise removal was performed using 3D
422 smoothing (kernel of 3) as morphological operation. Next, the binary mask was used to
423 extract the pores. Osteocyte lacunae were filled in a copy of the binary mask using a filling
424 morphological operation. Next, the multi-ROI conversion tool of Dragonfly was used to
425 select each lacuna individually. This tool allowed to define each osteocyte lacuna as an
426 individual ROI, hence enabling the calculation of each lacunae volume and shape. The
427 generated binary images were then used for the quantitative analysis of lacunae volume and
428 shape with Python software (version 3.5). The script used was written in a Jupyter notebook
429 with Python software (version 3.7). External libraries not contained in the Anaconda
430 environment were installed from their repository. Micropores smaller than 20 μm^3 and larger
431 than 3000 μm^3 were considered cracks or artifacts and excluded from the analysis. Two
432 separate lacunar volume ranges were investigated: small lacunae 20-900 μm^3 [44] and larger
433 lacunae 900-3000 μm^3.
434
435 4.5.2 Osteocyte lacunar volume analysis
436 For the osteocyte lacunar volume analysis, each segmented lacunar volume was calculated as
437 the total number of voxels times the volume of a single voxel. Based on this, we could define
438 the number of lacunae (Lc.N) of a given lacunar volume (Lc.V). We could also define the
439 total number of osteocyte lacunae (Lc.TN), total lacunar volume (Lc.TV) and trabecular bone
440 volume (Tb.BV). This nomenclature and units are summarized in Table 5.
441
442 4.5.3 Normalized lacunar volume frequency distribution and lacunar density
443 The lacunar volume frequency distributions were normalized to the trabecular bone volume
444 to account for size differences between samples, since larger samples have more lacunae than
445 smaller ones. For a given lacunar volume (Lc.V), we quantified the lacunar number (Lc.N),
446 normalized to the trabecular bone volume (Tb.BV) and excluding the total lacunar volume
447 (Tb.TV-Lc.TV). The data is presented as the frequency in a histogram with a bin size of
448 20 μm^3. Furthermore, the lacunar density was calculated as the total number of osteocyte
449 lacunae (Lc.TN) normalized to the trabecular bone volume and excluding lacunar total
450 volume (Tb.TV-Lc.TV), in other words, the summation of the osteocyte lacunar volume
451 frequency distribution. This was done for both ranges separately, small lacunae 20-900 μm^3
452 and larger lacunae 900-3000 μm^3.

453 4.5.4 Lacunar volume cumulative distribution

454 The cumulative distribution is calculated by sorting all osteocyte lacunae by volume, from
455 smallest to largest, and increasing the count of the fraction 1/N at each point, with N = length
456 of array. The cumulative lacunae volume distribution was plotted with respect to the lacunae
457 volume (Lc.V), with the x axis showing a given lacunae volume and the y axis showing the
458 cumulative volume. The 50% cutoff illustrating the specific volume below which half of all
459 osteocyte lacunae are contained, was marked with a dashed line.

460

461 4.5.5 Osteocyte lacunar microporosity analysis

462 The microporosity was calculated as the lacunar total volume (Lc.TV) divided by trabecular
463 total bone volume (Tb.TV) for each group. This was done for both ranges separately, small
464 lacunae 20-900 μm^3 and larger lacunae 900-3000 μm^3.

465

466 4.5.6 Osteocyte lacunar morphological analysis

467 To perform the lacunar morphological analysis, we defined the eigenvectors of an individual
468 lacuna with the corresponding major and minor axes. From the eigenvectors, the
469 corresponding eigenvalues (EV) were derived (EV1 > EV2 > EV3), where EV1 is the largest
470 eigenvalue and EV3 the smallest [45,46]. Three parameters were assessed to examine lacunae
471 morphology, based on the eigenvalues of each individual lacuna: the lacuna elongation,
472 flatness and anisotropy [30,31]. This nomenclature and units are summarized in Table 6.

473

474 **4.6 Statistical analysis**

475 A total of n=15 bone biopsy samples were analyzed, including MGUS n=3, SMM n=2, newly
476 diagnosed MM n=6 and control biopsy samples n=4 (Jamshidi n=1 and from autopsies n=3).
477 Additional bone biopsy samples (n>15) were collected but excluded from the analysis due to
478 lack of sample integrity (e.g. loss of bone structure (bone debris) during the extraction
479 procedure) or insufficient trabecular bone. To analyze changes in bone microporosity and
480 lacunar morphological analysis, a one-way analysis of variance (ANOVA) with Tukey's
481 multiple comparisons test (*$p<0.05$) was used (GraphPad Prism 8.0 software).

482

483 **5. Conflict of interest**

484 The authors declare no conflict of interest.

485

486 **6. Data availability**

The raw/processed data required to reproduce these findings are available in a publicly accessible repository of the Max Planck Society.

7. Author contributions

A Cipitria, I. Moreno-Jiménez and F. Jundt conceived the idea. I. Moreno-Jiménez and S. Heinig processed the bone biopsy samples and performed the experiments. D. Maichl collected and prepared the human Jamshidi bone biopsy samples. S. Strifler educated patients about and performed the biopsies, and collected clinical data. E. Leich-Zbat collected the human bone biopsy samples and clinical data; S. Blouin provided the control bone autopsy samples. I. Moreno-Jiménez, S. Heinig, U. Heras, F. Jundt and A. Cipitria analyzed the data. P. Fratzl and N. Fratzl-Zelman together with A Cipitria, I. Moreno-Jiménez and F. Jundt evaluated the methods and results. A Cipitria, I. Moreno-Jiménez and F. Jundt drafted the manuscript. All authors discussed the results and contributed to the final manuscript.

8. Funding

This research was funded by a postdoctoral research fellowship from the Humboldt Foundation (I.M.-J.) and by the Deutsche Forschungsgemeinschaft (DFG) Emmy Noether grant CI 203/2-1 (A.C). This work was supported by the Interdisciplinary Center for Clinical Research (IZKF), Medical Faculty of Würzburg, grant B-409 (F.J.) and the German Research Foundation (DFG) grants JU426/10-1 (F.J., 491715122) and JU 426/11-1 (F.J., 496963451). A.C. also thanks the funding from IKERBASQUE Basque Foundation for Science and from the Spanish Ministry of Science and Innovation (PID2021-123013OB-I00) (Ministerio de Ciencia e Innovación, la Agencia y del Fondo Europeo de Desarrollo Regional, Proyecto PID2021-123013OB-I00 financiado por MCIN/AEI/10.13039/501100011033/FEDER.UE).

9. Acknowledgements

The authors thank Daniel Werner, Jeannette Steffen, Daniela Garske and Susann Weichold at the Max Planck Institute of Colloids and Interfaces in Potsdam for their technical assistance.

References

1. Fratzl, P. & Weinkamer, R. Nature's hierarchical materials. *Prog Mater Sci* **52,** 1263–1334 (2007).
2. Bonewald, L. F. The amazing osteocyte. *Journal of Bone and Mineral Research* **26,** 229–238 (2011).

521 3. Gerbaix, M., Gnyubkin, V., Farlay, D., Olivier, C., Ammann, P., Courbon, G.,
522 Laroche, N., Genthial, R., Follet, H., Peyrin, F., Shenkman, B., Gauquelin-Koch, G. &
523 Vico, L. One-month spaceflight compromises the bone microstructure, tissue-level
524 mechanical properties, osteocyte survival and lacunae volume in mature mice
525 skeletons. *Sci Rep* **7,** 2659 (2017).
526 4. Lane, N. E., Yao, W., Balooch, M., Nalla, R. K., Balooch, G., Habelitz, S., Kinney, J.
527 H. & Bonewald, L. F. Glucocorticoid-treated mice have localized changes in
528 trabecular bone material properties and osteocyte lacunar size that are not observed in
529 placebo-treated or estrogen-deficient mice. *Journal of Bone and Mineral Research* **21,**
530 466–476 (2005).
531 5. Tiede-Lewis, L. M. & Dallas, S. L. Changes in the osteocyte lacunocanalicular
532 network with aging. *Bone* **122,** 101–113 (2019).
533 6. Tommasini, S. M., Trinward, A., Acerbo, A. S., De Carlo, F., Miller, L. M. & Judex,
534 S. Changes in intracortical microporosities induced by pharmaceutical treatment of
535 osteoporosis as detected by high resolution micro-CT. *Bone* **50,** 596–604 (2012).
536 7. Mullender, M. G., van der Meer, D. D., Huiskes, R. & Lips, P. Osteocyte density
537 changes in aging and osteoporosis. *Bone* **18,** 109–113 (1996).
538 8. Blouin, S., Misof, B. M., Mähr, M., Fratzl-Zelman, N., Roschger, P., Lueger, S.,
539 Messmer, P., Keplinger, P., Rauch, F., Glorieux, F. H., Berzlanovich, A., Gruber, G.
540 M., Brugger, P. C., Shane, E., Recker, R. R., Zwerina, J. & Hartmann, M. A.
541 Osteocyte lacunae in transiliac bone biopsy samples across life span. *Acta Biomater*
542 **157,** 275–287 (2023).
543 9. Milovanovic, P., Zimmermann, E. A., Riedel, C., Scheidt, A. vom, Herzog, L., Krause,
544 M., Djonic, D., Djuric, M., Püschel, K., Amling, M., Ritchie, R. O. & Busse, B. Multi-
545 level characterization of human femoral cortices and their underlying osteocyte
546 network reveal trends in quality of young, aged, osteoporotic and antiresorptive-treated
547 bone. *Biomaterials* **45,** 46–55 (2015).
548 10. Hemmatian, H., Bakker, A. D., Klein-Nulend, J. & van Lenthe, G. H. Aging,
549 osteocytes, and mechanotransduction. *Curr Osteoporos Rep* **15,** 401–411 (2017).
550 11. Hemmatian, H., Bakker, A. D., Klein-Nulend, J. & van Lenthe, G. H. Alterations in
551 osteocyte lacunar morphology affect local bone tissue strains. *J Mech Behav Biomed*
552 *Mater* **123,** 104730 (2021).
553 12. Mähr, M., Blouin, S., Behanova, M., Misof, B. M., Glorieux, F. H., Zwerina, J.,
554 Rauch, F., Hartmann, M. A. & Fratzl-Zelman, N. Increased Osteocyte Lacunae
555 Density in the Hypermineralized Bone Matrix of Children with Osteogenesis
556 Imperfecta Type I. *Int J Mol Sci* **22,** 4508 (2021).
557 13. Hedjazi, G., Guterman-Ram, G., Blouin, S., Schemenz, V., Wagermaier, W., Fratzl, P.,
558 Hartmann, M. A., Zwerina, J., Fratzl-Zelman, N. & Marini, J. C. Alterations of bone
559 material properties in growing Ifitm5/BRIL p.S42 knock-in mice, a new model for
560 atypical type VI osteogenesis imperfecta. *Bone* **162,** 116451 (2022).
561 14. Carriero, A., Doube, M., Vogt, M., Busse, B., Zustin, J., Levchuk, A., Schneider, P.,
562 Müller, R. & Shefelbine, S. J. Altered lacunar and vascular porosity in osteogenesis
563 imperfecta mouse bone as revealed by synchrotron tomography contributes to bone
564 fragility. *Bone* **61,** 116–124 (2014).
565 15. Atkinson, E. G. & Delgado-Calle, J. The emerging role of osteocytes in cancer in
566 bone. *JBMR Plus* **3,** e10186 (2019).
567 16. Adhikari, M. & Delgado-Calle, J. Role of osteocytes in cancer progression in the bone
568 and the associated skeletal disease. *Curr Osteoporos Rep* **19,** 247–255 (2021).

17. Hofbauer, L. C., Bozec, A., Rauner, M., Jakob, F., Perner, S. & Pantel, K. Novel approaches to target the microenvironment of bone metastasis. *Nat Rev Clin Oncol* **18,** 488–505 (2021).
18. Mastro, A. M., Gay, C. V., Welch, D. R., Donahue, H. J., Jewell, J., Mercer, R., DiGirolamo, D., Chislock, E. M. & Guttridge, K. Breast cancer cells induce osteoblast apoptosis: A possible contributor to bone degradation. *J Cell Biochem* **91,** 265–276 (2004).
19. Hemmatian, H., Conrad, S., Furesi, G., Mletzko, K., Krug, J., Faila, A. V., Kuhlmann, J. D., Rauner, M., Busse, B. & Jähn-Rickert, K. Reorganization of the osteocyte lacuno-canalicular network characteristics in tumor sites of an immunocompetent murine model of osteotropic cancers. *Bone* **152,** 116074 (2021).
20. Roodman, G. Pathogenesis of myeloma bone disease. *Blood Cells Mol Dis* **32,** 290–292 (2004).
21. Huston, A. & Roodman, G. D. Role of the microenvironment in multiple myeloma bone disease. *Future Oncology* **2,** 371–378 (2006).
22. Jacobsen, R. B. & Pharm, D. Diagnosis of smoldering multiple myeloma the TEMPI syndrome — A novel multisystem disease. *New England Journal of Medicine* 2011–2012 (2011).
23. Rajkumar, S. V., Dimopoulos, M. A., Palumbo, A., Blade, J., Merlini, G., Mateos, M.-V., Kumar, S., Hillengass, J., Kastritis, E., Richardson, P., Landgren, O., Paiva, B., Dispenzieri, A., Weiss, B., LeLeu, X., Zweegman, S., Lonial, S., Rosinol, L., Zamagni, E., Jagannath, S., Sezer, O., Kristinsson, S. Y., Caers, J., Usmani, S. Z., Lahuerta, J. J., Johnsen, H. E., Beksac, M., Cavo, M., Goldschmidt, H., Terpos, E., Kyle, R. A., Anderson, K. C., Durie, B. G. M. & Miguel, J. F. S. International myeloma working group updated criteria for the diagnosis of multiple myeloma. *Lancet Oncol* **15,** e538–e548 (2014).
24. Berenson, J., Rajdev, L. & Broder, M. Bone complications in multiple myeloma. *Cancer Biol Ther* **5,** 1082–1085 (2006).
25. Terpos, E., Ntanasis-Stathopoulos, I. & Dimopoulos, M. A. Myeloma bone disease: from biology findings to treatment approaches. *Blood* **133,** 1534–1539 (2019).
26. Callander, N. S. & Roodman, G. D. Myeloma bone disease. *Semin Hematol* **38,** 276–285 (2001).
27. Delgado-Calle, J., Anderson, J., Cregor, M. D., Hiasa, M., Chirgwin, J. M., Carlesso, N., Yoneda, T., Mohammad, K. S., Plotkin, L. I., Roodman, G. D. & Bellido, T. Bidirectional notch signaling and osteocyte-derived factors in the bone marrow microenvironment promote tumor cell proliferation and bone destruction in multiple myeloma. *Cancer Res* **76,** 1089–1100 (2016).
28. Ziouti, F., Soares, A. P., Moreno-Jiménez, I., Rack, A., Bogen, B., Cipitria, A., Zaslansky, P. & Jundt, F. An early myeloma bone disease model in skeletally mature mice as a platform for biomaterial characterization of the extracellular matrix. *J Oncol* **2020,** 1–12 (2020).
29. Palumbo, A., Avet-Loiseau, H., Oliva, S., Lokhorst, H. M., Goldschmidt, H., Rosinol, L., Richardson, P., Caltagirone, S., Lahuerta, J. J., Facon, T., Bringhen, S., Gay, F., Attal, M., Passera, R., Spencer, A., Offidani, M., Kumar, S., Musto, P., Lonial, S., Petrucci, M. T., Orlowski, R. Z., Zamagni, E., Morgan, G., Dimopoulos, M. A., Durie, B. G. M., Anderson, K. C., Sonneveld, P., San Miguel, J., Cavo, M., Rajkumar, S. V. & Moreau, P. Revised International Staging System for Multiple Myeloma: A Report From International Myeloma Working Group. *Journal of Clinical Oncology* **33,** 2863–2869 (2015).

30. El Bialy, I., Jiskoot, W. & Reza Nejadnik, M. Formulation, delivery and stability of bone morphogenetic proteins for effective bone regeneration. *Pharm Res* **34,** 1152–1170 (2017).
31. Chaumel, J., Schotte, M., Bizzarro, J. J., Zaslansky, P., Fratzl, P., Baum, D. & Dean, M. N. Co-aligned chondrocytes: Zonal morphological variation and structured arrangement of cell lacunae in tessellated cartilage. *Bone* **134,** 115264 (2020).
32. Goff, E., Cohen, A., Shane, E., Recker, R. R., Kuhn, G. & Müller, R. Large-scale osteocyte lacunar morphological analysis of transiliac bone in normal and osteoporotic premenopausal women. *Bone* **160,** 116424 (2022).
33. Milovanovic, P. & Busse, B. Phenomenon of osteocyte lacunar mineralization: indicator of former osteocyte death and a novel marker of impaired bone quality? *Endocr Connect* **9,** R70–R80 (2020).
34. Delgado-Calle, J., Bellido, T. & Roodman, G. D. Role of osteocytes in multiple myeloma bone disease. *Curr Opin Support Palliat Care* **8,** 407–413 (2014).
35. Tsourdi, E., Jähn, K., Rauner, M., Busse, B. & Bonewald, L. F. Physiological and pathological osteocytic osteolysis. *J Musculoskelet Neuronal Interact* **18,** 292–303 (2018).
36. Jähn, K., Kelkar, S., Zhao, H., Xie, Y., Tiede-Lewis, L. M., Dusevich, V., Dallas, S. L. & Bonewald, L. F. Osteocytes acidify their microenvironment in response to PTHrP in vitro and in lactating mice in vivo. *Journal of Bone and Mineral Research* **32,** 1761–1772 (2017).
37. Kogawa, M., Wijenayaka, A. R., Ormsby, R. T., Thomas, G. P., Anderson, P. H., Bonewald, L. F., Findlay, D. M. & Atkins, G. J. Sclerostin regulates release of bone mineral by osteocytes by induction of carbonic anhydrase 2. *Journal of Bone and Mineral Research* **28,** 2436–2448 (2013).
38. Tang, S. Y., Herber, R.-P., Ho, S. P. & Alliston, T. Matrix metalloproteinase-13 is required for osteocytic perilacunar remodeling and maintains bone fracture resistance. *Journal of Bone and Mineral Research* **27,** 1936–1950 (2012).
39. Schemenz, V., Gjardy, A., Chamasemani, F. F., Roschger, A., Roschger, P., Zaslansky, P., Helfen, L., Burghammer, M., Fratzl, P., Weinkamer, R., Brunner, R., Willie, B. M. & Wagermaier, W. Heterogeneity of the osteocyte lacuno-canalicular network architecture and material characteristics across different tissue types in healing bone. *J Struct Biol* **212,** 107616 (2020).
40. Vlot, M. C., den Heijer, M., de Jongh, R. T., Vervloet, M. G., Lems, W. F., de Jonge, R., Obermayer-Pietsch, B. & Heijboer, A. C. Clinical utility of bone markers in various diseases. *Bone* **114,** 215–225 (2018).
41. Schwarzer, R., Nickel, N., Godau, J., Willie, B. M., Duda, G. N., Schwarzer, R., Cirovic, B., Leutz, A., Manz, R., Bogen, B., Dörken, B. & Jundt, F. Notch pathway inhibition controls myeloma bone disease in the murine MOPC315.BM model. *Blood Cancer J* **4,** e217–e217 (2014).
42. Rummler, M., Ziouti, F., Bouchard, A. L., Brandl, A., Duda, G. N., Bogen, B., Beilhack, A., Lynch, M. E., Jundt, F. & Willie, B. M. Mechanical loading prevents bone destruction and exerts anti-tumor effects in the MOPC315.BM.Luc model of myeloma bone disease. *Acta Biomater* **119,** 247–258 (2021).
43. Ziouti, F., Rummler, M., Steyn, B., Thiele, T., Seliger, A., Duda, G. N., Bogen, B., Willie, B. M. & Jundt, F. Prevention of bone destruction by mechanical loading is not enhanced by the Bruton's tyrosine kinase inhibitor CC-292 in myeloma bone disease. *Int J Mol Sci* **22,** 3840 (2021).

44. McCreadie, B. R., Hollister, S. J., Schaffler, M. B. & Goldstein, S. A. Osteocyte lacuna size and shape in women with and without osteoporotic fracture. *J Biomech* **37,** 563–572 (2004).
45. Gescheidtova, E., Marcon, P., Bartusek, K., Gescheidtová, E., Marcon, P. & Bartusek, K. Visualization of plant fibres via diffusion tensor imaging. in *PIERS Proceedings, Suzhou, China* (2011).
46. Mader, K. S., Schneider, P., Müller, R. & Stampanoni, M. A quantitative framework for the 3D characterization of the osteocyte lacunar system. *Bone* **57,** 142–154 (2013).

676 **Figures and captions**

677 **Figure 1**

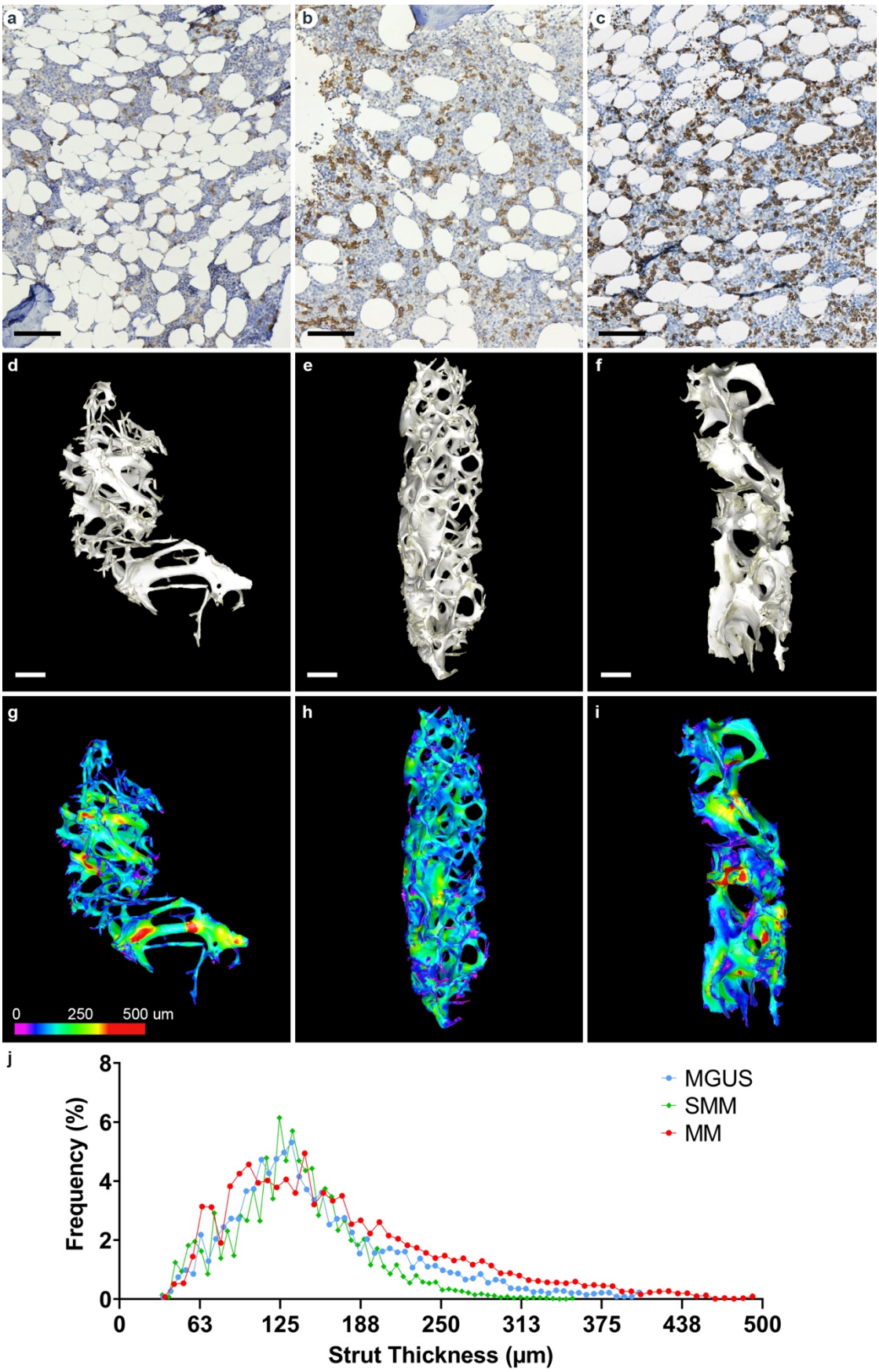

678

679 **Figure 1. Immunohistochemical (IHC) CD138 staining and low resolution microCT**
680 **overview of the bone biopsies from patients with: (a, d, g) monoclonal gammopathy of**
681 **undetermined significance (MGUS), (b, e, h) smoldering myeloma (SMM), and (c, f, i)**
682 **newly diagnosed multiple myeloma (MM).** (a-c) Representative light microscopy images of
683 the bone marrow compartment from the biopsy samples: CD138 positive staining in brown,
684 cell nuclei counterstain in blue. (d-f) 3D renders of low resolution (7 µm voxel) microCT
685 scans of representative bone biopsies. (g-i) Quantitative analysis of trabecular bone strut
686 thickness distribution and color code visualization with Dragonfly software. (j) Frequency
687 distribution of strut thickness. Scale bars equal to 100 µm (a-c), 1 mm (d-f).
688

Figure 2

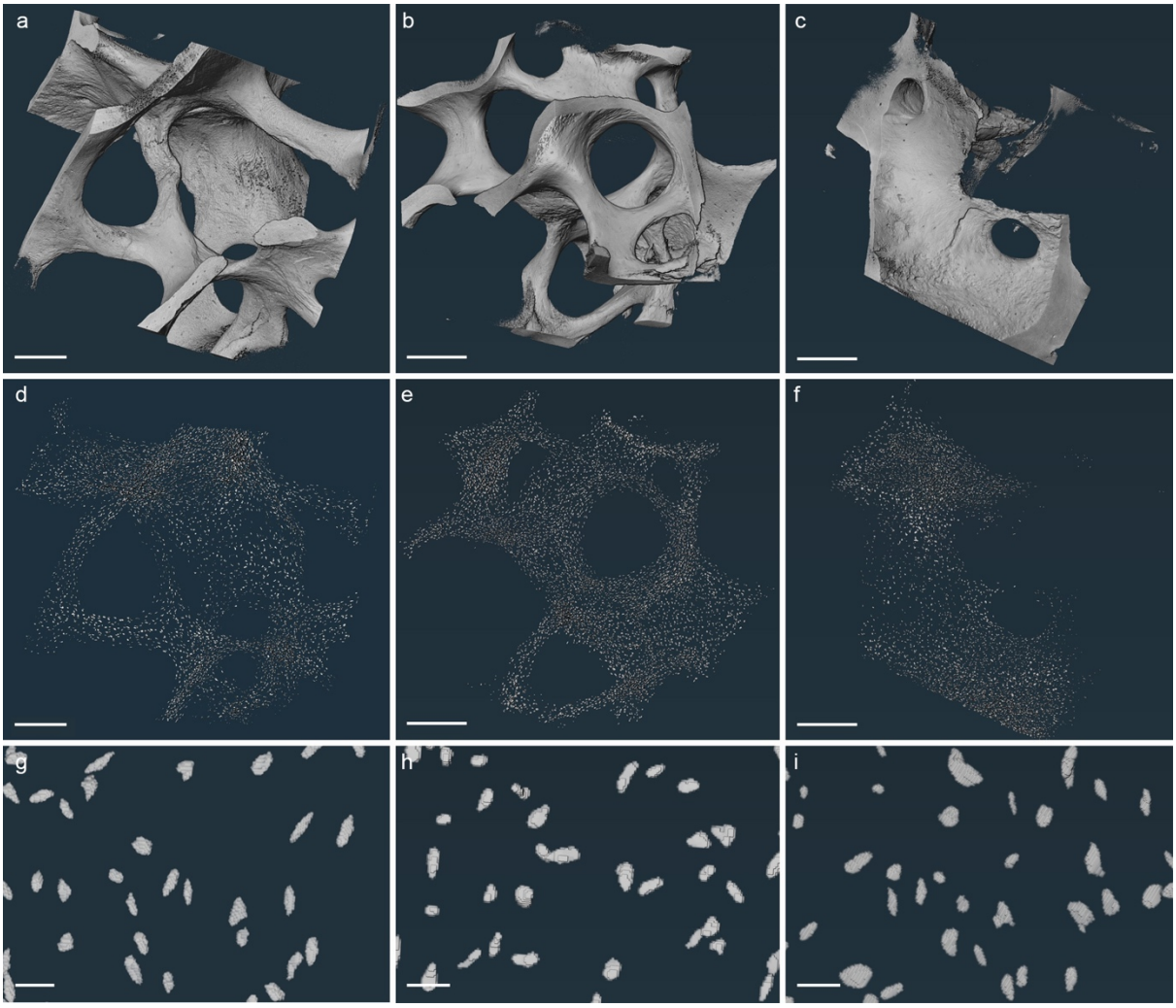

Figure 2. Bone biopsy macroscopic structure and osteocyte lacunar microporosity visualized with high resolution microCT. (a-c) 3D rendering of local scans (high resolution microCT; voxel size 1-2 µm) and (d-f) the corresponding segmented osteocyte lacunar microporosity of representative samples: (a, d, g) MGUS bone biopsy #MGUS 2, (b, e, h) SMM bone biopsy #SMM 1, (c, f, i) MM bone biopsy #MM 1. Scale bars equal to 250 µm (a, d), 350 µm (b, e), 400 µm (c, f) and 20 µm (g-i).

698 **Figure 3**

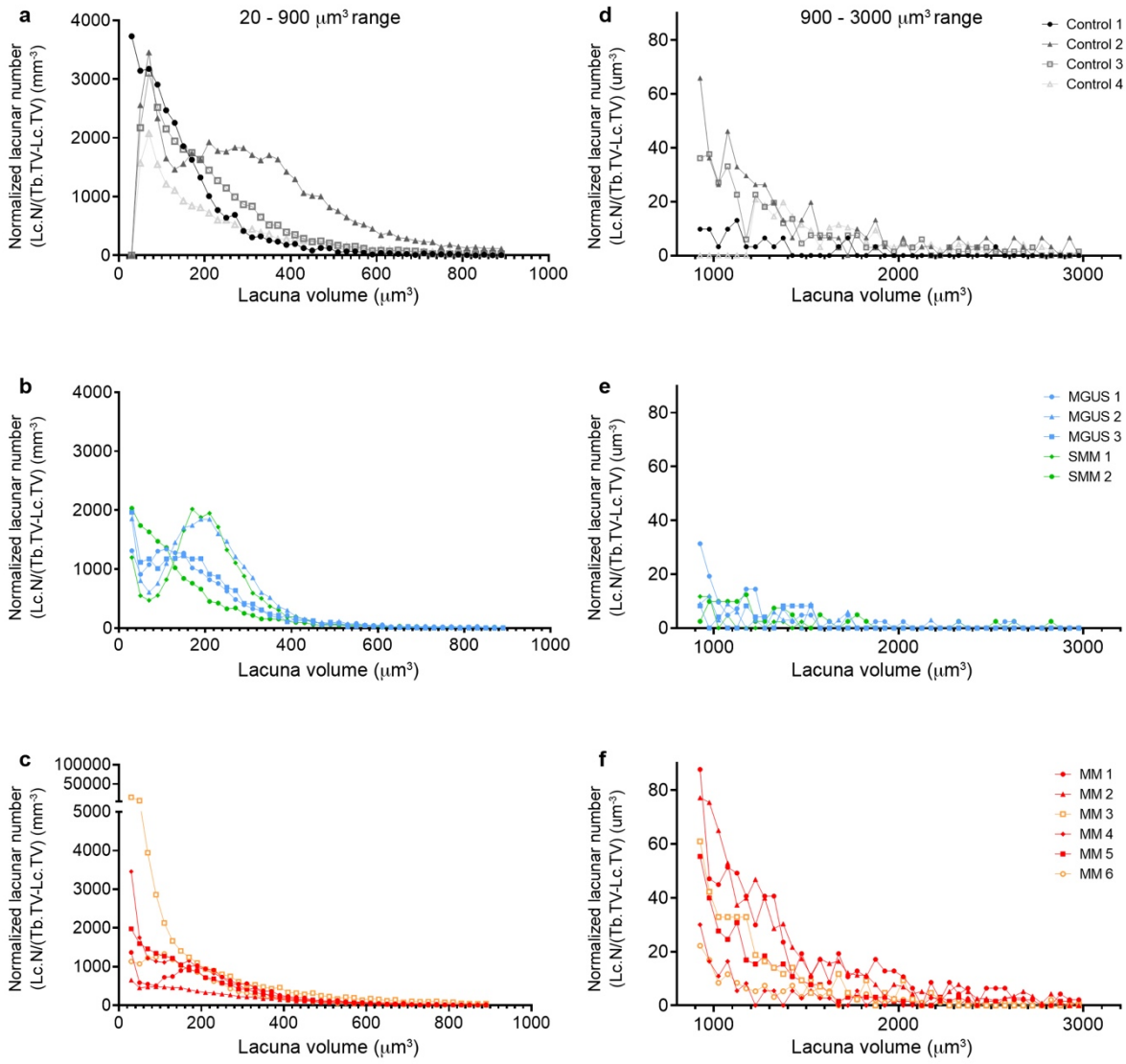

699

700 **Figure 3. Lacunar volume frequency distribution**. Frequency distribution normalized to
701 trabecular bone volume for two separate lacunar volume ranges: 20-900 µm³ and 900-3000
702 µm³. For each lacunae volume interval (x-axis), number of osteocyte lacunae (Lc.N)
703 normalized by the trabecular total bone volume excluding lacunar total volume (Tb.TV-Lc-
704 TV) (y-axis). Frequency distribution for each group: (a, d) control, (b, e) MGUS and SMM,
705 (c, f) MM. Sample from the Jamshid biopsy in black, all other control samples in grey.
706 MGUS in blue, SMM in green, MM samples with bone lytic lesion in red, MM samples
707 without lytic lesions in orange.

708

709 **Figure 4**

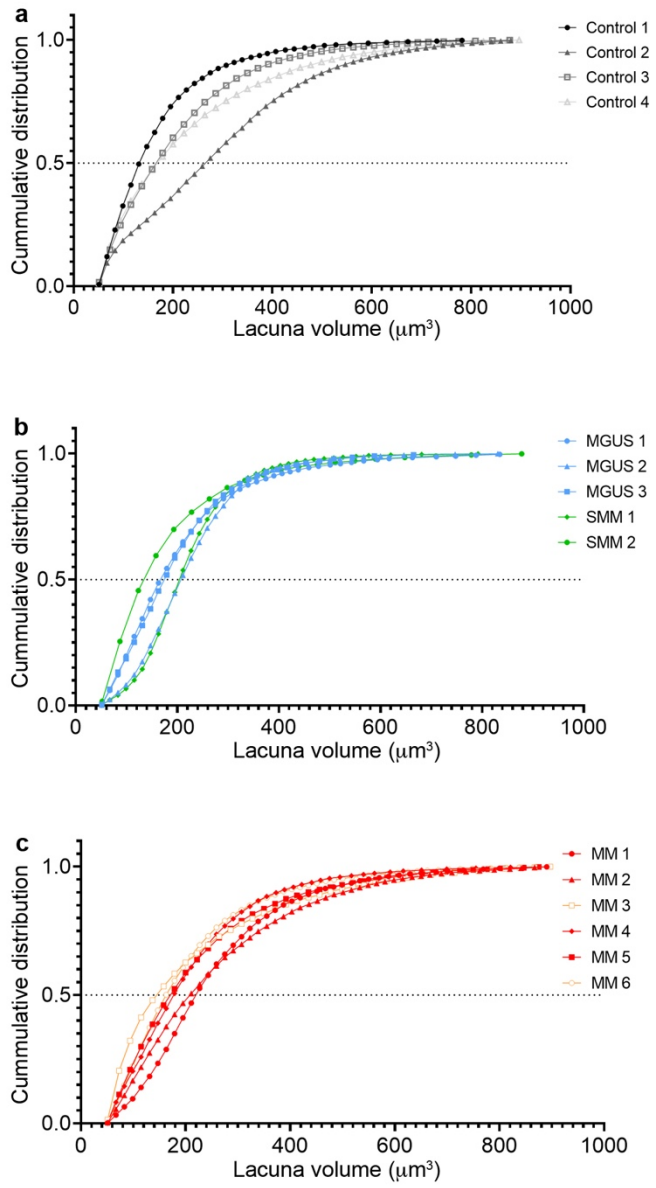

710

711 **Figure 4. Lacunar volume cumulative distribution for the small lacunae 20-900 µm³**
712 **range.** Cumulative distribution (from 0 to 1) of lacunae (y-axis) for each volume in µm³ (x-
713 axis). Cumulative distribution for each group: (a) control, (b) MGUS and SMM, (c) MM.
714 Dashed line indicates the 50% cutoff volume below which are half of all osteocyte lacunae of
715 one sample. Sample from the Jamshid biopsy in black, all other control samples in grey.
716 MGUS in blue, SMM in green, MM samples with bone lytic lesion in red, MM samples
717 without lytic lesions in orange.

718

719 **Figure 5**

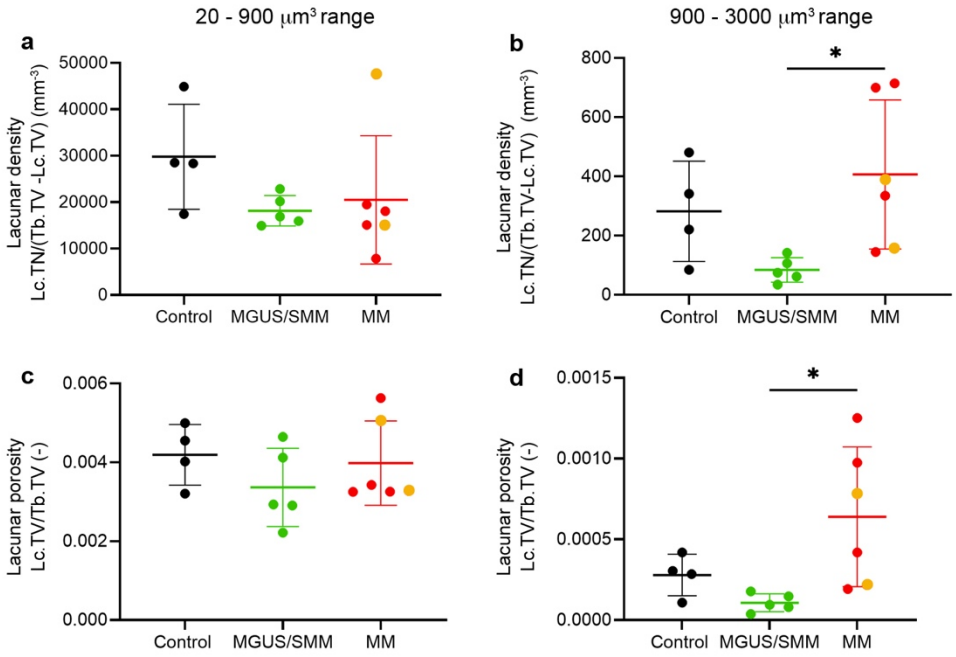

720

721 **Figure 5. Lacunar density and microporosity analysis for the small lacunae 20-900 µm³**
722 **range and for the larger lacunae 900-3000 µm³ range**. Lacunar density calculated as the
723 total number of osteocyte lacunae (Lc.TN) normalized to the trabecular bone volume and
724 excluding lacunar total volume (Tb.TV-Lc.TV), for each group control, MGUS/SMM and
725 newly diagnosed MM (samples with bone lytic lesion in red, samples without lytic lesions in
726 orange). Microporosity calculated as lacunar total volume (Lc.TV) divided by trabecular total
727 bone volume (Tb.TV) for each group. Error bars indicate mean ± SD. One way ANOVA with
728 Tukey's multiple comparison test *$p<0.05$.

729

730 **Figure 6**

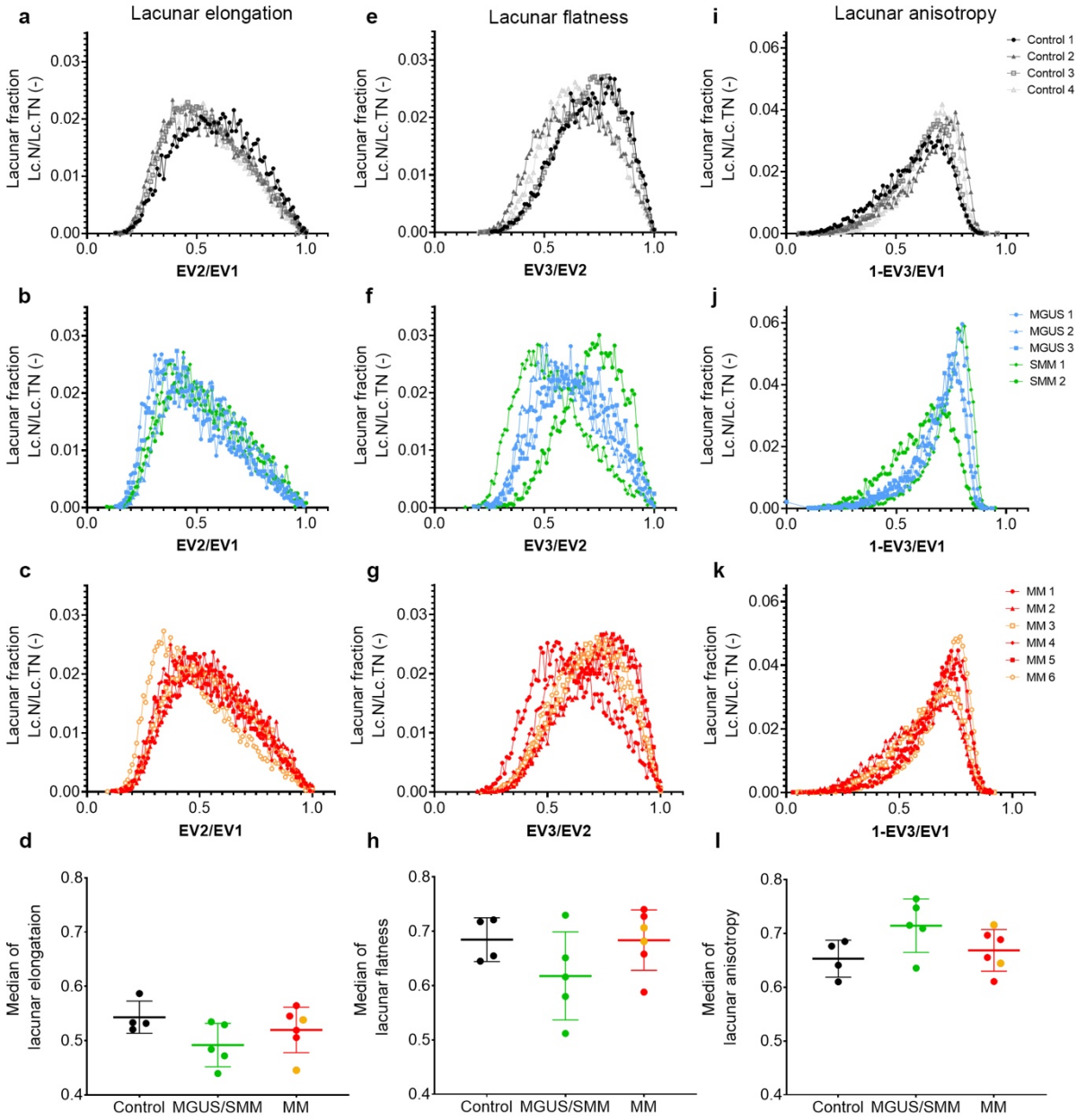

731

732 **Figure 6. Lacunar morphological analysis for the small lacunae 20-900 µm³ range.**
733 Lacunae elongation, flatness and anisotropy analysis for (a, e, i) control, (b, f, j)
734 MGUS/SMM and (c, g, k) MM groups. Individual lacunae were assigned with eigenvalues
735 (EV1, EV2 and EV3) to then calculate lacuna elongation as EV2/EV1 (with lower values for
736 elongated and 1 for spherical) as (a-c) lacunar fraction (Lc.N/Lc.TN) and as (d) median of all
737 lacuna elongation values for each sample; lacuna flatness as EV3/EV2 (ranging from 0 for
738 flat to 1 for spherical) as (e-g) lacunar fraction (Lc.N/Lc.TN) and as (h) median of all lacuna
739 flatness values for each sample; and lacuna anisotropy as 1-EV3/EV1 (with smaller values
740 for isotropic/spherical and 1 for highest anisotropy) as (i-k) lacunar fraction (Lc.N/Lc.TN)

741 and as (l) median of all lacuna anisotropy values for each sample. Sample from the Jamshid
742 biopsy in black, all other control samples in grey. MGUS in blue, SMM in green, MM
743 samples with bone lytic lesion in red, MM samples without lytic lesions in orange. Error bars
744 indicate mean ± SD.
745
746

747 **Tables**

748 **Table 1. Clinical data from MGUS patients from the University Hospital Würzburg**

Parameters			
biopsy number	MGUS 1	MGUS 2	MGUS 3
age (years)	71	60	68
gender	f	m	f
immunoglobulin subtype	IgG lambda	IgG kappa	IgG kappa
r-ISS	not applicable	not applicable	not applicable
cytogenetic risk	not applicable	not applicable	not applicable
M-protein [g/L]	not detectable	not detectable	1,2
heavy chain [mg/dL, normal range]	1382 (610-1616)*	881 (610-1616)	507 (610-1616)
involved serum free light chain (sFLC) [mg/L, normal range]	23,89 (5,71-26,30)	10,75 (3,30-19,40)	215 (3,30-19,40)
ratio (involved / uninvolved sFLC)	0,86	1,02	5,44
bone marrow infiltration of $CD138^+$ cells [%]	<10	<10	<5
CT findings of osteolytic lesion	none	none	none
hemoglobin [g/dL]	12,9 (12-16)	14,4 (13,5-16,9)	12,7 (12-16)
creatinine [mg/dL]	0,63 (0-0,95)	1,06 (0-1,17)	6,69 (0-0,95)
cytogenetics**	no aberration	no aberration	no aberration
calcium [mmol/L]	2,2 (2,0-2,7)	2,5 (2,0-2,7)	2,3 (2,0-2,7)
alkaline phosphatase [U/L]	51 (35-105)	72 (35-105)	not available
inorganic phosphate [mmol/L]	1,09 (0,87-1,45)	1 (0,87-1,45)	1,85 (0,87-1,45)
bone anti-resorption treatment (duration)	Denosumab (four months)	no	no

749 * Values in brackets show the normal range for the parameters, respectively

750 ** Cytogenetic alterations by fluorescence in situ hybridization (FISH)

751

752 **Table 2. Clinical data from SMM patients from the University Hospital Würzburg**

Parameters		
biopsy number	SMM 1	SMM 2
age (years)	46	70
gender	f	m
immunoglobulin subtype	IgA kappa	IgA lambda
r-ISS	II	I
cytogenetic risk	high risk	standard risk
M-protein [g/L]	not detectable	13,42
heavy chain [mg/dL, normal range]	1826 (88-410)	2826 (88-410)
involved serum free light chain (sFLC) [mg/L, normal range]	11,82 (3,30-19,40)	54,99 (5,71-26,3)
ratio (involved / uninvolved sFLC)	1,33	12,03
bone marrow infiltration of $CD138^+$ cells [%]	10-15	20-30
CT findings of osteolytic lesion	none	none
hemoglobin [g/dL]	12 (12-16)	13,2 (13,5-16,9)
creatinine [mg/dL]	0,78 (0-0,95)	0,91 (0-1,17)
cytogenetics	t4;14, gain of 1q21	del13q14
calcium [mmol/L]	2,2 (2,0-2,7)	2,4 (2,0-2,7)
alkaline phosphatase [U/L]	59 (35-105)	40 (35-105)
inorganic phosphate [mmol/L]	1,08 (0,87-1,45)	1,23 (0,87-1,45)
bone anti-resorption treatment (duration)	not known	no

753

754

755 **Table 3. Clinical data from newly diagnosed MM patients from the University Hospital**
756 **Würzburg**

Parameters			
biopsy number	MM 1	MM 2	MM 3
age (years)	58	57	72
gender	m	m	f
immunoglobulin subtype	IgG kappa	kappa	IgG lambda
r-ISS	III	II	III
cytogenetic risk	high risk	standard risk	high risk
M-protein [g/L]	35,3	not detectable	20,6
heavy chain [mg/dL, normal range]	4765 (610-1616)	not available	3074 (610-1616)
involved serum free light chain (sFLC) [mg/L, normal range]	71,12 (3,30-19,40)	8260 (3,30-19,40)	1376 (5,71-26,3)
ratio (involved / uninvolved sFLC)	40,41	890,09	355,56
bone marrow infiltration of $CD138^+$ cells [%]	70	60-70	90
CT findings of osteolytic lesion	osteolytic lesion with extraosseous soft tissue mass in spine (T12), lytic lesion in pelvis, rib series fractures, medullary lesions in femora and humeri, reduced bone mineral density	disseminated osteolysis in spine, one large lesion in T9 with increased fracture risk, old vertebral body collapse in T7 and fracture of the fourth left rib, multiple small osteolyses in scapulae, ribs, sternum reduced bone mineral density	no osteolytic lesions medullary lesions in upper and lower limbs, spine, sternum; reduced bone mineral density
hemoglobin [g/dL]	10,8 (13,5-16,9)	10,7 (13,5-16,9)	10,2 (12-16)
creatinine [mg/dL]	0,83 (0-1,17)	2,3 (0-1,17)	0,72 (0-0,95)
cytogenetics	t14;16, gain of 1q21	t11;14	del 17p, 1q gain, del14q, del 4p, del 16q, del 5p
calcium [mmol/L]	2,3 (2,0-2,7)	2,9 (2,0-2,7)	2,5 (2,0-2,7)
alkaline phosphatase [U/L]	97 (35-105)	80 (35-105)	49 (35-105)
inorganic phosphate [mmol/L]	1,25 (0,87-1,45)	1,33 (0,87-1,45)	0,99 (0,87-1,45)

bone anti-resorption treatment (duration)	bisphosphonate (zoledronic acid) for one month	no	no

757

758 **Table 3 (cont). Clinical data from newly diagnosed MM patients from the University**
759 **Hospital Würzburg**

Parameters			
biopsy number	MM 4	MM 5	MM 6
age (years)	60	68	64
gender	m	f	f
immunoglobulin subtype	IgA lambda	IgG kappa	IgG kappa
r-ISS	II	II	II
cytogenetic risk	standard risk	standard risk	standard risk
M-protein [g/L]	32,6	4,5	7,4
heavy chain (mg/dL, normal range)	4000 (88-410)	1180 (610-1616)	1625 (610-1616)
involved serum free light chain (sFLC) [mg/L, normal range]	33,8 (5,71-26,3)	16,59 (3,30-19,40)	309,8 (3,30-19,40)
ratio (involved / uninvolved sFLC)	4,26	1,49	8,41
bone marrow infiltration of $CD138^+$ cells [%]	30	50	60
CT findings of osteolytic lesion	osteolytic lesion in pelvis; mild reduction in bone mineral density	disseminated osteolysis in skull, spine, fracture series in spine (T7, 8, 11; L1, 2, 4), reduced bone mineral density in spine	none
hemoglobin [g/dL]	14 (13,5-16,9)	10,1 (12-16)	12,8 (12-16)
creatinine [mg/dL]	0,96 (0-1,17)	1,02 (0-0,95)	0,91 (0-0,95)
cytogenetics	del 1p32, del13q14, gain of 1q21	trisomy 11	gain of 1q21
calcium [mmol/L]	2,4 (2,0-2,7)	2,5 (2,0-2,7)	2,4 (2,0-2,7)
alkaline phosphatase [U/L]	41 (35-105)	95 (35-105)	92 (35-105)
inorganic phosphate [mmol/L]	1,19 (0,87-1,45)	0,94 (0,87-1,45)	0,74 (0,87-1,45)
bone anti-resorption treatment (duration)	no	no	no

760

761 **Table 4. Control samples: Jamshidi bone biopsy from a patient at the University**
762 **Hospital Würzburg and samples from autopsies at the Ludwig Boltzmann-Institute of**
763 **Osteology, Vienna.**

Parameters				
biopsy number	control 1	control 2	control 3	control 4
type of biopsy	jamshidi	autopsy*	autopsy*	autopsy*
age (years)	69	64	57	63
gender	f	f	f	f
previous disease	myelodysplastic syndrome	not known	not known	not known

764 * Subset of an earlier cohort presented previously [8] and re-evaluated here

765
766 **Table 5. Nomenclature for osteocyte lacunar volume analysis**

Nomenclature	**Abbreviation**	**Unit**
Number of osteocyte lacunae	Lc. N	-
Total number osteocyte lacunae	Lc. TN	-
Lacunar volume	Lc. V	µm³
Total lacunar volume	Lc. TV	µm³
Trabecular bone volume	Tb. BV	µm³

767
768
769 **Table 6: Nomenclature for osteocyte lacunar morphological analysis**

Parameter	**Definition**	**Unit**	**Formula**
Normalized lacunar volume frequency distribution	Number of lacunae volume divided by the trabecular bone total volume minus the lacuna total volume	#/µm³	$\frac{\Sigma\, Lc.N}{Tb.TV\ -\ Lc.TV}$
Lacunar volume cumulative distribution	Sorted sum of volume divided by total volume	-	
Microporosity	Total lacunar volume with respect to the total trabecular bone volume	-	$\frac{Lc.TV}{Tb.TV}$
Lacuna elongation	0 for elongated 1 for spherical	-	$\frac{EV2}{EV1}$
Lacuna flatness	0 for flat 1 for spherical	-	$\frac{EV3}{EV2}$
Lacuna anisotropy	0 for isotropic, spherical 1 for highly anisotropic	-	$1 - \frac{EV3}{EV1}$

770